

COMPUTED AXIAL LITHOGRAPHY FOR RAPID VOLUMETRIC 3D ADDITIVE MANUFACTURING

Brett E. Kelly^{1,3}, Indrasen Bhattacharya², Maxim Shusteff³, Hayden K. Taylor¹, and
Christopher M. Spaddacini³

¹Department of Mechanical Engineering, University of California, Berkeley. Berkeley,

²Department of Applied Science and Technology, University of California, Berkeley

³Materials Engineering Division, Lawrence Livermore National Laboratory

Abstract

The vast majority of additive manufacturing processes today operate by printing voxels serially point-by-point to build up a 3D part. In some higher throughput techniques, for example optical printing methods such as projection stereolithography [1], [2], parts are printed layer-by-layer by curing full 2D (very thin in one dimension) layers of the 3D part in each print step. In this work, we demonstrate a new technique which prints entire parts all at once and eliminates layering. The approach, termed Computed Axial Lithography (CAL), is based on tomographic reconstruction, with mathematical optimization to generate a set of projections to optically define an arbitrary dose distribution within a target volume and to cure the entire volume simultaneously. Volume-at-once fabrication of complex geometries is achieved using a custom system built from a DLP projector and a rotating resin volume. This technique can be used to expand the range of printable geometries in additive manufacturing and relax constraints on factors such as overhangs in topology optimization. The method also vastly increases print speed for 3D parts. We show complex and overhanging geometries printed in situ without layering.

Introduction

Additive manufacturing (AM) technology has expanded greatly since the inception of stereolithography in the 1980s. Today, AM techniques are used in a variety of fields to print structures that often could not be manufactured by conventional subtractive processes. Applications range from biological scaffolds for culturing tissue in vitro [3] to micro-architected materials with microstructures designed to produce enhanced or novel material properties [4]. Most AM methods today operate in one of a series of forms which we can categorize by the geometric complexity of their unit print operation, or the geometry of the material that is printed in a single print step. A majority of printing methods today rely on a print step which is either zero or one-dimensional. Zero-dimensional (0D) print operations include those where material is formed or processed at a single point within the print volume. Methods such as selective laser sintering (SLS), selective laser melting (SLM), stereolithography (SLA) and inkjet printing fall into this category. Another large subset of methods exist which rely on a unit print operation which is one dimensional (1D), or which print a line in the unit operation. These techniques include, most prominently, extrusion-based methods such as fused deposition

modeling (FDM) and direct ink writing (DIW). Recently, more and more techniques are emerging which use a two-dimensional (2D) unit print operation. These techniques are mostly optical and include projection stereolithography methods [1] and Continuous Liquid Interface Production (CLIP) [2]. The aforementioned 0D, 1D, and 2D unit operation printing methods generally achieve printing of 3D geometries by repeating their unit print operations serially in the remaining dimension(s). In the 2D case, this involves repeating the operation once for sequential thin cross-sections or “layers” of the part. Recently, the authors of this work introduced a technique capable of printing entire 3D parts in a single step [5]. This technique was based on the use of intensity superposition of beams from three orthogonal directions to photopolymerize a 3D geometry in situ in a single print step. It introduced a new paradigm of volumetric fabrication which provides a number of potential advantages over layer-by-layer printing. However, the three beam superposition technique, while a useful demonstration of the ability to print volumes at once, is constrained in the range of 3D geometries it can print to those that can be formed by intersecting three orthogonal images. This paper introduces a new technique, Computed Axial Lithography (CAL), which preserves the ability to form entire parts at once in situ, but greatly expands the geometric flexibility.

The ability to print full 3D parts volumetrically, with a three-dimensional unit print operation, offers a number of advantages over layered printing. To start, the CAL technique has already demonstrated the ability to print 3D parts faster than layered methods. In a 15mm x 15mm x 15mm print volume, the complex parts in Figures 8A and 8C were printed in under 8 minutes while the sphere geometry in Figure 8B was printed in just 80 seconds. More interestingly, volumetric printing offers unique potential advantages in the ability to print geometries that cannot be printed layer-by-layer. These geometries include those which require support material in layered printing, such as geometries with overhangs and the geometry demonstrated in Figure 8A. Finally, by printing parts all at once, rather than in sequential layers, mechanical anisotropies arising from layering can be reduced or eliminated.

The CAL approach described in this work is founded on the generation of an accumulated 3D intensity distribution designed carefully in conjunction with photocuring chemistry such that in a single unit operation with a single development step, a 3D part of arbitrary user-defined geometry is generated. It is rooted in the basic concepts of computed tomographic (CT) imaging [6], which we apply to stereolithography.

CAL Printing Algorithm

Rather than printing the target 3D geometry layer-by-layer, the CAL method is designed to expose the transparent resin by projecting 2D images from an array of angles about an azimuthal axis. A major component of this research was the development of a computational algorithm to design the projected image from each angle based on a target 3D geometry. The optical design method for CAL is based on one of the possible reconstruction procedures in computed tomography (CT). Prior art in a similar technique exists in intensity modulated radiation therapy (IMRT) for cancer treatment [7]. IMRT seeks to produce a 3D variation of radiation dose in a target volume in the patient's body. Typical practice in this radiotherapy procedure involves the projection of a small number (7-10) of 2D distributions of X-ray pencil beams at a few selected angles. The intensity of

the beamlets is chosen to satisfy a set of therapeutic constraints including: sufficient but not excessive dosage in the tumor, low radiation dose in certain critical organs as well as the physical constraint that radiation dose must be positive. This is a challenging inverse problem, for which iterative optimization techniques have yielded success in defining previously impossible dosage distributions, including concave regions such as the prostate gland. Producing dose distributions in a clinically reasonable timeframe while satisfying multiple objectives continues to be an area of active research. From a mathematical perspective, the volumetric 3D printing problem has similarities in terms of constraints, but greater freedom in the exact dose distribution because of the non-linear thresholding behavior of the photoresins used.

To describe the optical design algorithm, it is easiest to start by reducing the problem of generating 2D projections to print a 3D geometry to that of generating 1D projections to print a 2D geometry. Consider the 2D geometry to be a slice of the full 3D part. This 2D flatland analysis is then readily extended to the third dimension by concatenating calculated 1D projections for subsequent slices of the 3D part. Note that this technique is still distinctly different from layered printing as neighboring layers form simultaneously rather than sequentially. In the raytracing picture used in this algorithm, we consider all the beams for a particular projection angle to be parallel. This is analogous to parallel beam tomography in the medical community. In the CT imaging configuration where a uniform pencil beam at azimuthal angle θ is projected into the 2D imaging volume with optical density given by $R(x, y)$, the collected dose distribution on the 1D camera along the space dimension x is given by $P(x, \theta)$:

$$P(x, \theta) = \int R(x \cos \theta - u \sin \theta, x \sin \theta + u \cos \theta) du \quad (1)$$

where $(-u \sin \theta, u \cos \theta)$ for parameter u represents a line through the origin in the direction of exposure for the particular angle θ . $P(x, \theta)$ is the well known Radon transform of the 2D image R . We will refer to $P(x, \theta)$ as the angular projections of the image. From the projection slice theorem, it turns out that the Fourier transform of a projection at angle θ is exactly equal to a 1D sample of the original image's 2D Fourier transform $R(k_x, k_y)$. The 1D sample is taken along a slice $(k \cos \theta, k \sin \theta)$ corresponding to the particular angle at which the projection was integrated. This can be expressed as:

$$\int P(x, \theta) e^{-ikx} dx = R(k \cos \theta, k \sin \theta) \quad (2)$$

This is illustrated in Figure 1, where 1D cuts in the projection space image can be compared to similarly shaded central slices in the Fourier domain. Sufficiently dense sampling in the Fourier domain is required for an accurate CT image reconstruction.

Tomographic image computation geometry

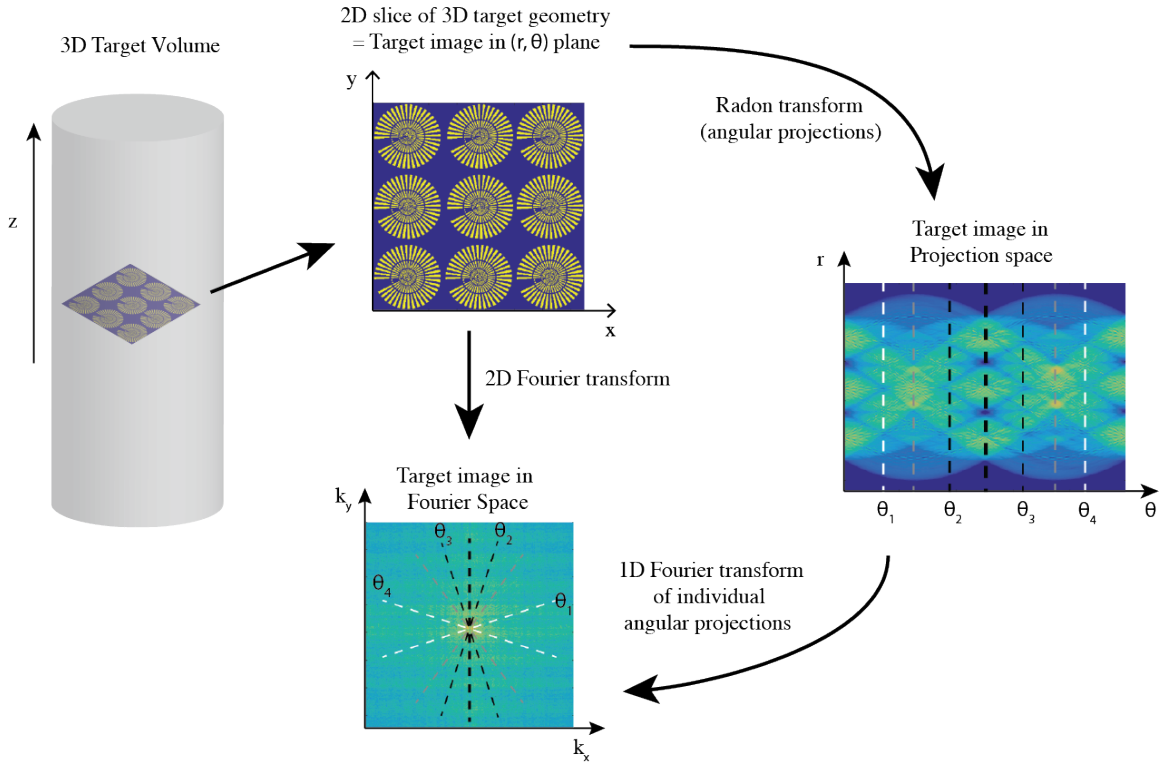


Figure 1 – Representation of Fourier slicing and sampling based on angular projections from many angles

The reconstruction of the 2D image volume can be understood as an algorithmic time reversal of the CT imaging process. This back-projection algorithm starts with the measured 1D projections and propagates each individual projection backwards while uniformly exposing the target region with this intensity pattern. This is repeated for every angle. From the central slice theorem, this corresponds to building up the sample slice by slice in the Fourier domain. This algorithmic back-projection then motivates a technique to physically back-project the computed Radon transform at each angle and directly construct desired 3D dose volumes. However, directly back-projecting the 2D radon transform will not produce the correct result. In order to compensate for the inverse radial oversampling inherent in the Fourier slicing approach, we apply a radially increasing ramp filter. We also apply a window to the ramp filter in the Fourier domain, so as to exclude high spatial frequencies beyond the degree of sampling provided by the number of angular samples. IMRT literature suggests an exponential windowing filter for a smooth backprojection filter. This approach leads to the following backprojection filter in the Fourier domain (k, θ) :

$$H(k) = |k|e^{-\left(\frac{k}{k_0}\right)^4} \quad (3)$$

where k_0 is chosen based on the number of angular samples. This windowed high pass filter is applied on every Fourier slice before back-propagating it to form the image. The spatial domain representation of the filter has negative ripples that often lead to the backprojections being negative even if the projections themselves are positive. This is a challenge since the backprojections are physically constrained to positive values. We address this initially in two ways: 1) by adding a constant offset to all projections to raise the minimum value to zero, or 2) by setting all negative projection values to zero. We then use this set of projections as an initialization step for a constrained optimization procedure.

The goal of the optimization algorithm is to calculate the set of backprojections $P_{opt}(x, \theta)$ that best produces a desired output intensity. We use an iterative optimization procedure based on projected gradient descent. This method is guaranteed to converge for a convex objective and convex constraint set. Neither of these is true in our case due to the thresholding property of the resin and discrete values for the projector input. However, this heuristic performs quite well for some simple geometries, and reasonably well for more complicated ones. One iteration of the optimization loop to generate $P_{n+1}(x, \theta)$ from $P_n(x, \theta)$ given a target image $R(x, y)$ goes as follows (illustrated in Figure 2):

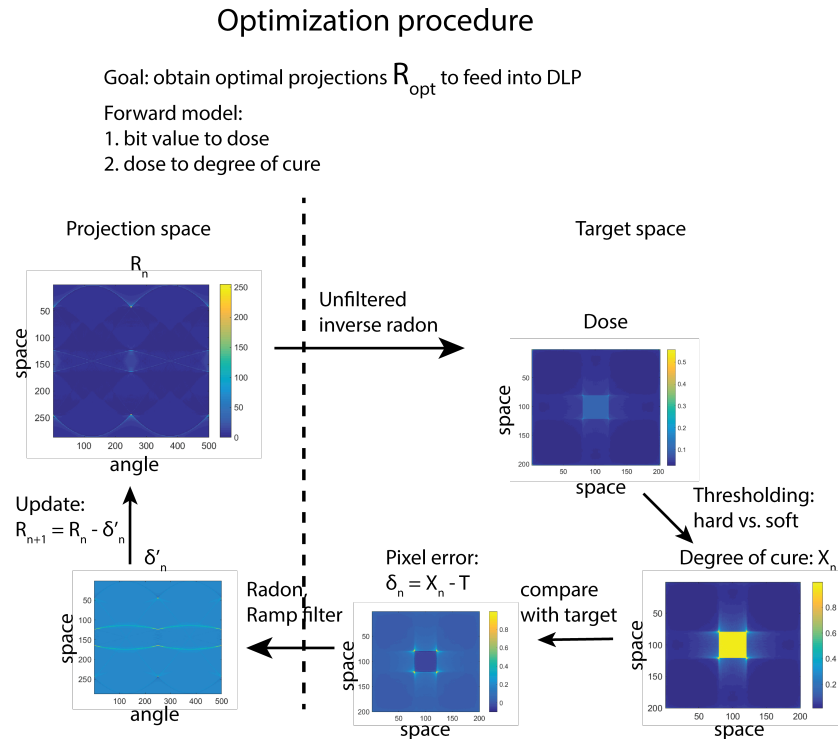


Figure 2 - The optimization flow, with example images corresponding to each stage in the algorithm.

1) *Projection*: Starting with the 8-bit DLP projections $P_n(x, \theta)$ computationally generate an unthresholded 2D dose distribution of power $D(x, y)$. This requires an accurate understanding and calibration of the system’s forward model. The relationship between specified pixel brightness values and the resulting projected intensity is extracted from measurements taken with a calibrated silicon photodiode. We assume, for now, a

chemical model where regions which receive more than a critical threshold dose form solid, crosslinked material while those with less than the critical dose remain uncrosslinked and are later developed away. A future implementation will directly solve photopolymerization rate equations integrated over time and space to generate the degree of crosslinking in the forward model.

2) *Thresholding*: Depending on the development recipe, convert the degree of crosslinking to the thresholded image at the n th iteration $R_n(x, y)$. We have experimented with variations of this procedure, to prevent the optimization from being sensitive to a single threshold, and instead have attempted to penalize absolute errors around the threshold as well. In all cases however, $R_n(x, y)$ lies between 0 and 1, representing material fully washed away as opposed to fully present

3) *Error*: We determine the error in the image by comparing with the target: $\delta_n(x, y) = R_n(x, y) - R(x, y)$. We transform this into the backprojection domain by performing a Radon transform (integral projection) at every angle, followed by ramp filtering. This leads to the projection domain error $\delta'_n(x, \theta)$

4) *Update*: An unconstrained new set of projections is computed as: $R_{n+1}(x, \theta) = R_n(x, \theta) - \delta'_n(x, \theta)$. Finally, the computed projection is constrained to positive 8-bit values by first setting negatives to zero, and then quantizing. It can be confirmed that the updated $R_{n+1}(x, \theta)$ is the closest element in the constrained set to the computed unconstrained value and is therefore a projection

Algorithm Validation

As an incremental step before applying the optical design algorithm toward 3D CAL printing, a physical validation of the algorithm was performed. For this validation, an

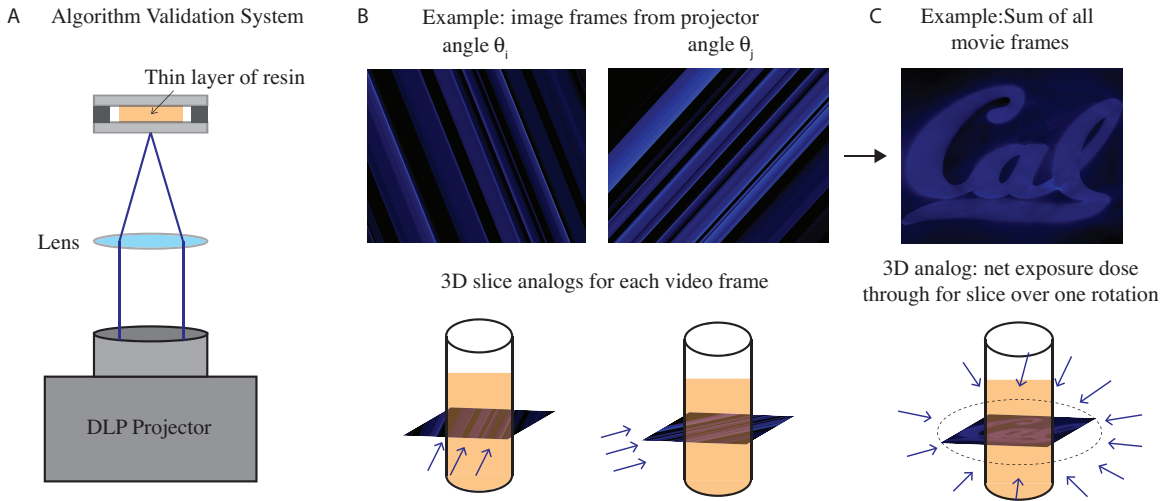


Figure 3 - A: Physical system used to validate optical design algorithm. B: Example movie frames from projected video and representation of analogy to 3D system. Each frame corresponds to the dose passing through the resin from a particular angle θ . C: Example sum of movie frames from all angles. This dosage distribution is analogous to the net exposure dose seen by a horizontal slice of the 3D volume over one rotation.

experimental apparatus was constructed as depicted in Figure 3A. In this apparatus, a DLP projector was used as the optical source to generate the projections. The system was configured such that a 2D image was incident on a thin layer of resin. The video output from the projector was set to match the time-evolving intensity map which would be incident upon a cross-section of the 3D volume in the 3D CAL system. Thus, each video frame corresponded to a 1D projection propagated in a single direction dictated by angle of illumination from the algorithm as depicted in Figure 3B. As designed by the algorithm, the sum of all video frames gives an image which approximates the target geometry. An example is shown in Figure 3C.

The algorithm was tested for a range of geometries. Projections from 500 evenly spaced angles about 360° were computed and used to generate the video frames. The frame rate of the projected movie was set to simulate an angular rotation of $25^\circ/\text{s}$ to match the max rotational speed of the rotating stage used later in the 3D CAL printing system. This setup yielded useful results to validate the algorithm. Example print results are shown in Figure 4.

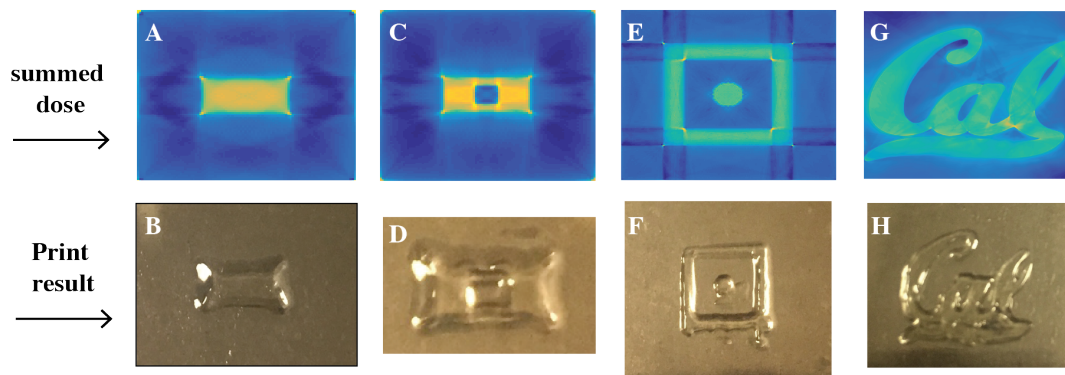


Figure 4 - Algorithm validation results. For four geometries, the summed dose from all angles and the corresponding print results are shown A-B: a geometry with sharp edges. C-D: a geometry with a void inside of a solid object. E-F: a geometry with a solid piece inside another solid piece. G-H: a complex geometry with curved features.

Extension to 3D

In order to translate the optical design algorithm from 2D validation to 3D printing, additional physical effects must be considered. These effects arise from the fact that in 3D, the projections from each angle propagate through the resin volume and encounter attenuation and changes in refractive index. The algorithm does not currently account for these effects, although it soon will. Rather than accounting for these effects in the algorithm, we have addressed them in the design of the photoresin. First, rather than modelling attenuation in the algorithm, we sought to minimize it. This was achieved by carefully selecting the photoinitiator concentration used in the resin. Based on the photoinitiator concentration in the resin, a tradeoff exists between intensity uniformity and print speed. A low photoinitiator concentration minimizes absorption and preserves

intensity uniformity of the projection through the volume, but also leads to slower print times. The slow print time, however, can be counteracted by using higher intensity. In the prints shown in this work, two photoinitiators were used: Irgacure 819 and Camphorquinone (CQ). The absorption spectra of each of these constituents were measured on a UV-Vis spectrophotometer and are plotted in Figure 5, along with the spectral output of the blue channel of the DLP projector used.

To address the change in refractive index, we rely on the geometry being defined during the oxygen inhibition phase of polymerization [8],[9]. During the oxygen inhibition phase, generated photoradicals quench local oxygen molecules faster in regions of higher dose. At the onset of curing, when the optical properties begin to change, the geometry has already been defined through spatially localized depletion of oxygen. Since a large fraction of the optical dose is used to define local regions that are free of oxygen, we may say that much of the 3D printing process is invisible to the eye. This has the advantage that parts that have been ‘printed’ already do not lead to significant optical scattering as the process continues.

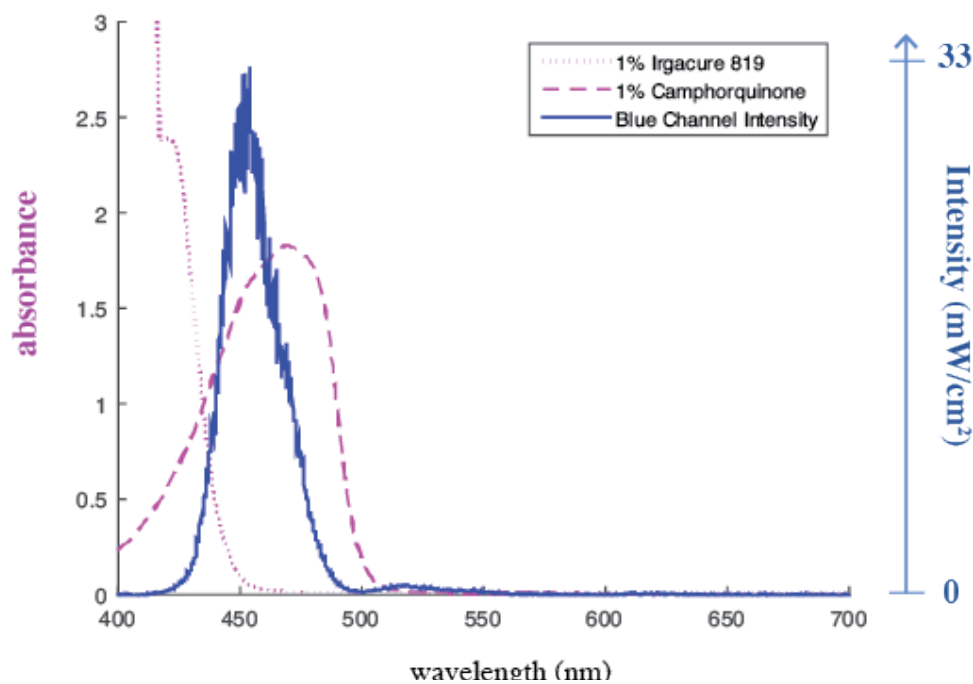


Figure 5 – Absorption spectra of the two photoinitiator molecules used in this work plotted against the spectral output of the DLP projector used.

The final effects that arise in the 3D printing case but not in the 2D algorithm validation case are the emergence of gravitational, buoyant, and centripetal forces as the curing part increases in density compared to the uncured resin. To minimize the effect of forces exerted on the curing part, a high viscosity resin was formulated. The polymer used in this resin comprised of a mix of 75 wt% Bisphenol A glycerolate (1 glycerol/phenol) diacrylate and 25 wt% PEGDA 250 Da. The viscosity was measured using cone and plate rheometry to be ~4000 cP and independent of shear rate. All polymer constituents and photoinitiators were obtained from Sigma Aldrich.

CAL 3D Printing

In order to demonstrate the ability of CAL to print 3D parts, a 3D printing system was constructed. This system is depicted in Figure 6A. The same DLP projector was used as the optical source to generate the projections. A cylindrical glass vial was used to contain the resin. This vial was fixed from the top to a controlled rotating stage. In the printing system, the image output of the projector is synchronized to the rotation of the vial. The image projected at a particular angle contains a concatenation of 1D projections for each vertical slice of the target geometry to form a 2D image as shown in Figure 6B, where each frame is the image output from the algorithm for a particular angle. To avoid cylindrical lensing effects which distort the incident image, a rectangular box filled with a fluid of refractive index > 1 was used. In this work, the index-matching fluid used was the same prepolymer composition used in the resin but without the photoinitiator added.

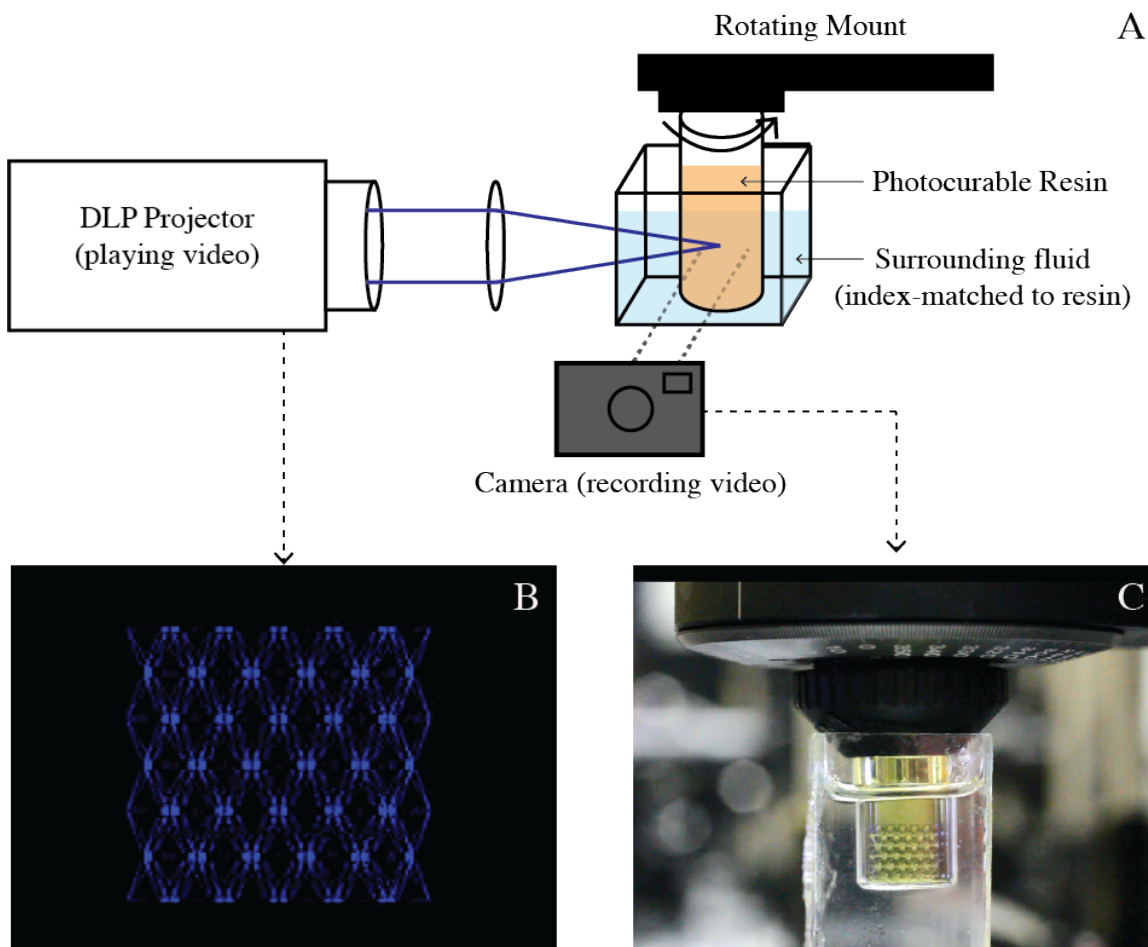


Figure 6 - CAL 3D printing system. A: full system schematic. B: an example of an image frame output from the projector for a particular angle. C: an image of a 3D structure forming inside the system.

Using the 3D CAL printing system, successful 3D prints of various geometries were achieved. As a first example, parts with uniform vertical cross-section were printed. In these parts, the algorithmic design of the projections for each vertical slice is the same, making the computation simpler and faster. These results are shown in Figure 7. The first geometry, a rectangular prism, demonstrates the potential of CAL to print 3D geometries with sharp corners. Another geometry, with a semicircle cross-section, demonstrates the ability to simultaneously print curved surfaces, flat surfaces, and corners. Most importantly, successful printing of a hollow cylinder demonstrates the ability to print voids within a solid structure.

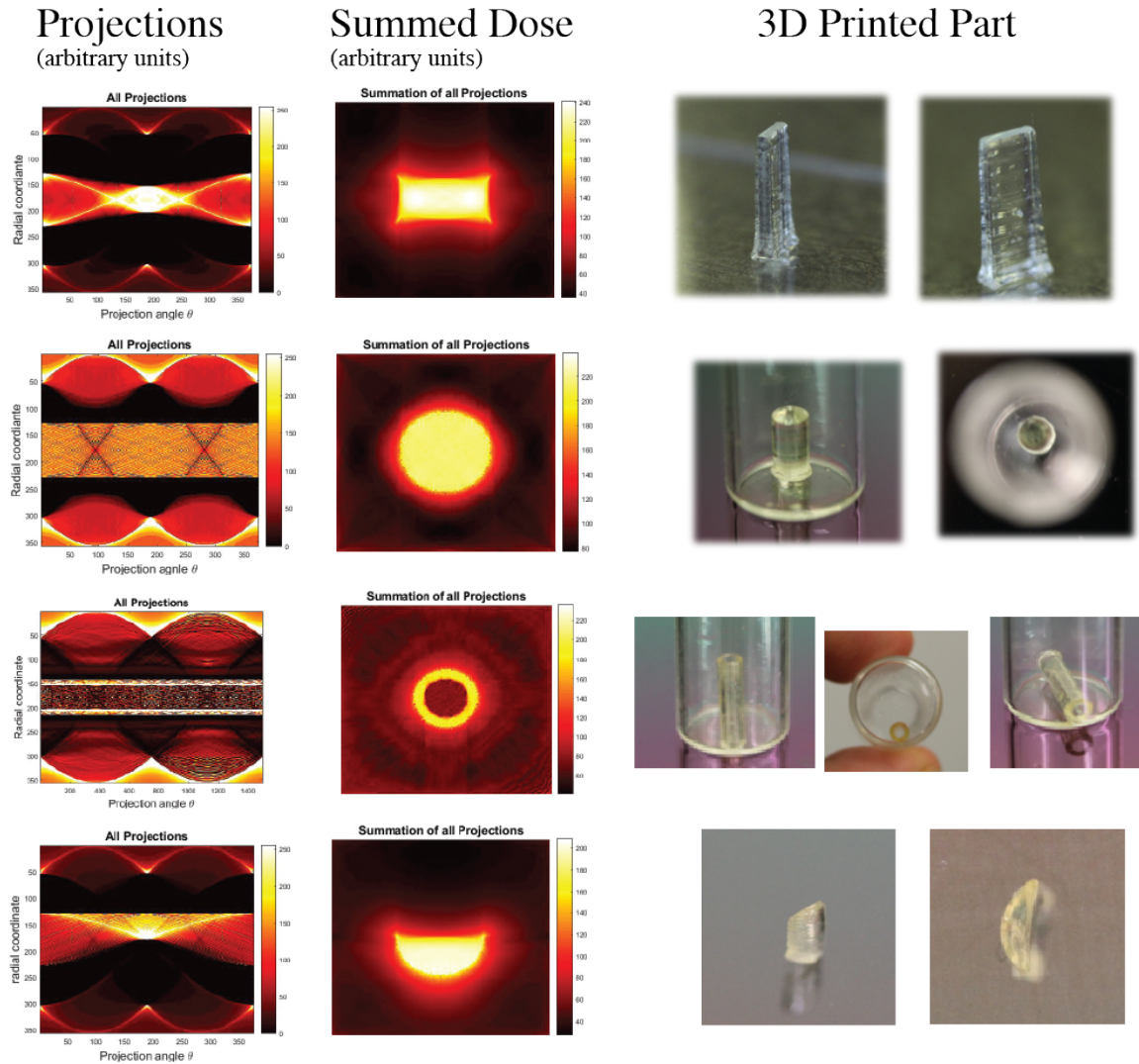


Figure 7 - 3D CAL-printed results with constant cross-section in z. Column 1: 1D projections vs. angle for each z slice. Column 2: summed intensity distribution from all projections in each z slice. Column 3. Images of 3D printed results

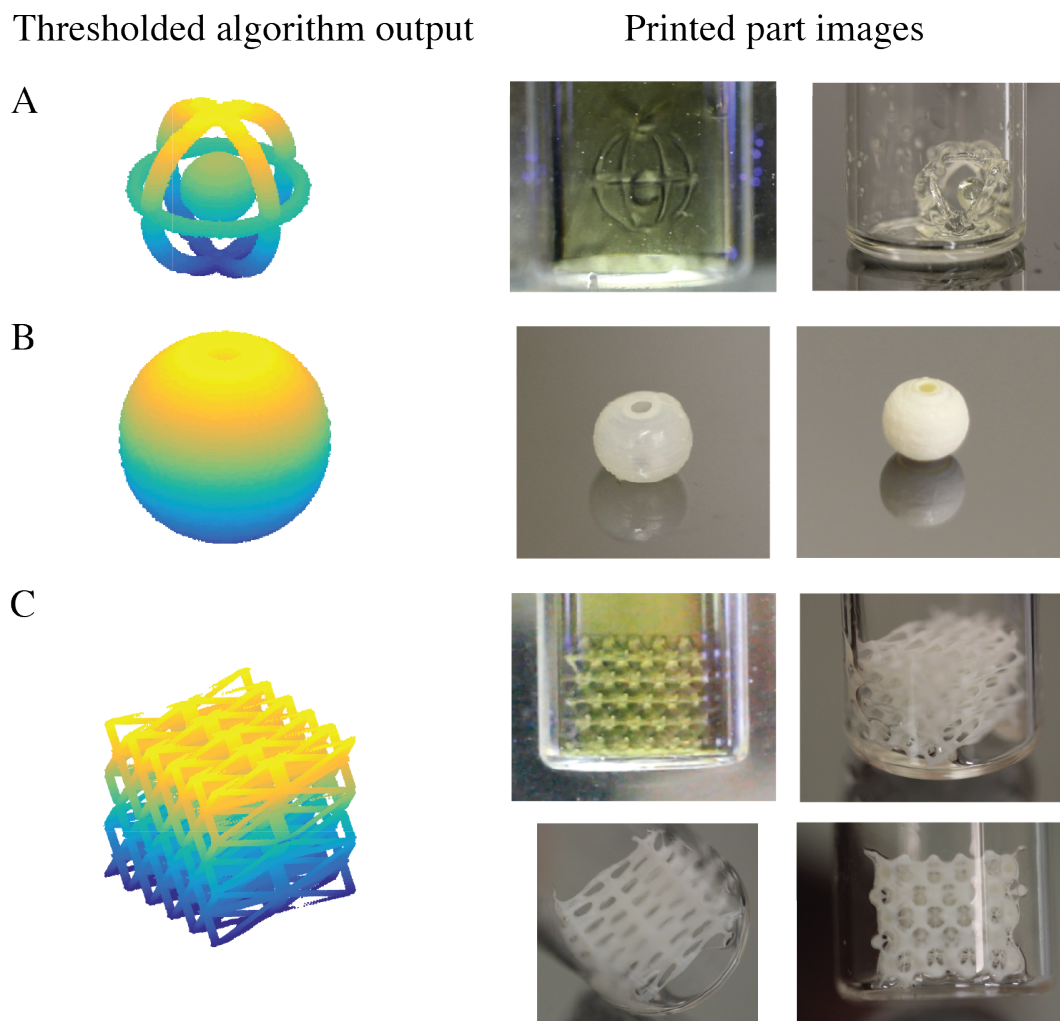


Figure 8 - Examples of 3D printed parts with non-uniform cross-section. Algorithm output is shown as a point cloud, plotting points where the net exposure dose exceeds a threshold. Color represents the axial (z) coordinate for printing.

After successful printing of uniform cross-section 3D parts, more complex parts with non-uniform cross-section were printed. These results are shown in Figure 7. The ball-in-a-cage part shown in Figure 8A demonstrates an example of the ability of CAL to print geometries which cannot be printed by layer-by-layer methods without support material. The octet truss structure in Figure 8C demonstrates the ability of CAL to print complex structures that can only be manufactured additively.

Discussion

The present work demonstrates a careful design and initial implementation of an additive manufacturing system which can promote a new paradigm in the way such systems are designed and operate. It fosters a shift from the conventional approach of building 3D parts layer-by-layer toward an approach which is designed to address the entire volume of the 3D geometry. This method can present advantages in manufacturing throughput as well as in the ability to print overhanging geometries without the need for mechanical support material. To further fuel this shift, there are some modifications to the prototyped system that will be implemented in future work. First, some improvements can be made by the design of a system where the resin volume is static and the optics rotate around it. The advantage of this system design is that the optics can be rotated at a much higher speed than the volume. This arises from the constraint of fluid motion in the resin volume at higher rotation speeds. The only constraints on the speed with which the optics can be rotated are motor rotation speed limits and the minimum frame rate of the optical system. Neither limit has been nearly approached in the current system. Finally, a future implementation of this system could be designed such that projections from all angles are generated simultaneously. Such a system could then achieve true single step printing of complex 3D geometries.

Acknowledgements

This work was performed under the auspices of the U.S. Department of Energy of Lawrence Livermore National Laboratory under Contract DE-AC52-07NA27344. This work was performed under LDRD funding 14-SI-004, and 17-ERD-116. This document has been released under IM review # LLNL-PROC-733997. We would like to thank both the Center for Engineered Materials and Manufacturing at Lawrence Livermore National Laboratory and the Design for Nanomanufacturing group at the University of California, Berkeley. We would also like to acknowledge useful discussions with Robert Panas, Allison Browar, James Oakdale, and Ryan Hensleigh at LLNL as well as with Prof. Laura Waller, Jingzhao Zhang and Prof. Ren Ng at Berkeley.

References

- [1] X. Zheng, J. Deotte, M. P. Alonso, G. R. Farquar, T. H. Weisgraber, S. Gemberling, H. Lee, N. Fang, and C. M. Spadaccini, "Design and optimization of a light-emitting diode projection micro-stereolithography three-dimensional manufacturing system," *Rev. Sci. Instrum.*, vol. 83, no. 2012, pp. 0–6, 2012.
- [2] J. R. Tumbleston, D. Shirvanyants, N. Ermoshkin, R. Januszewicz, A. R. Johnson, D. Kelly, K. Chen, R. Pinschmidt, J. P. Rolland, A. Ermoshkin, E. T. Samulski, and J. M. Desimone, "Continuous Liquid Interface Production of 3D Objects," *Science (80-.)*, vol. 347, no. 6228, pp. 1349–1352, 2015.
- [3] B. Derby, "Printing and Prototyping of Tissues and Scaffolds," *Science (80-.)*, vol. 338, no. 6109, pp. 921–926, 2012.
- [4] X. Zheng, H. Lee, T. H. Weisgraber, M. Shusteff, J. DeOtte, E. B. Duoss, J. D. Kuntz, M. M. Biener, Q. Ge, J. a Jackson, S. O. Kucheyev, N. X. Fang, and C. M.

- Spadaccini, "Ultralight, ultrastiff mechanical metamaterials.," *Science*, vol. 344, pp. 1373–7, 2014.
- [5] M. Shusteff, R. M. Panas, J. Henriksson, B. E. Kelly, A. E. M. Browar, N. X. Fang, and C. M. Spadaccini, "Additive Fabrication of 3D Structures by Holographic Lithography," in *Proceedings of the 27th Annual Solid Freeform Fabrication Symposium*, 2016, pp. 1183–1192.
- [6] A. C. Kak and M. Slaney, *Principles of Computerized Tomographic Imaging*. Society of Industrial and Applied Mathematics, 2001.
- [7] T. Bortfeld, J. Bürkelbach, R. Boesecke, and W. Schlegel, "Methods of image reconstruction from projections applied to conformation radiotherapy," *Phys. Med. Biol.*, vol. 35, no. 10, pp. 1423–1434, 1990.
- [8] A. K. O'Brien and C. N. Bowman, "Impact of oxygen on photopolymerization kinetics and polymer structure," *Macromolecules*, vol. 39, no. 7, pp. 2501–2506, 2006.
- [9] D. Dendukuri, P. Panda, R. Haghgooie, J. M. Kim, T. A. Hatton, and P. S. Doyle, "Modeling of oxygen-inhibited free radical photopolymerization in a PDMS microfluidic device," *Macromolecules*, vol. 41, pp. 8547–8556, 2008.